

# Investigation of Different Oxygen Partial Pressures on MgGa<sub>2</sub>O<sub>4</sub>-Resistive Random-Access Memory

Yu-Neng Kao, Wei-Lun Huang, Sheng-Po Chang,\* Wei-Chih Lai, and Shoou-Jinn Chang

Cite This: *ACS Omega* 2023, 8, 3705–3712

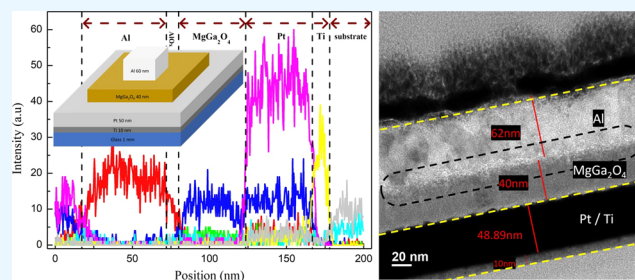
Read Online

ACCESS |

Metrics &amp; More

Article Recommendations

**ABSTRACT:** Different oxygen partial-pressure MgGa<sub>2</sub>O<sub>4</sub>-resistive RAMs (RRAMs) are fabricated to investigate the resistive switching behaviors. The X-ray photoelectron spectroscopy results, set voltage, reset voltage, cycling endurance, and retention time are drawn for comparison. With the increasing oxygen ratio gas flow, the resistive switching characteristics of MgGa<sub>2</sub>O<sub>4</sub> RRAM are drastically elevated by changing the fabrication conditions of the RS layer. Moreover, we portray a filament model to explain the most likely mechanism associated with the generation and rupture of conductive filaments composed of oxygen vacancies. The formation of the interfacial layer (AlO<sub>x</sub>) and the participation of the Joule heating effect are included to explain the highly distributed high-resistance state (HRS). The high randomness among switching cycles for memory application should be prevented, but it is suitable for the physical unclonable function. The relationship between HRS and the next time set voltage shows a strong correlation, and the conduction mechanisms of the low-resistance state (LRS) and HRS correspond to ohmic conduction and space charge-limited conduction, respectively. Meanwhile, the RRAM undergoes 10,000 s retention tests, and the two resistance states can be distinguished without obvious alternation or degradation. A favorable cycling endurance and retention time achieved by optimizing the fabrication parameters of Al/MgGa<sub>2</sub>O<sub>4</sub>/Pt RRAM have the potential for nonvolatile memristors and information security applications.



## INTRODUCTION

With the prosperous development of artificial intelligence and the Internet of Things, it is urgent that high-density nonvolatile memory be developed to keep up with low-power consumption requirements and data storage demand. The volatile memories (SRAM and DRAM) with fast speeds in writing and reading (SRAM) and are extremely dense (DRAM) lose the data when the power supply is switched off.<sup>1</sup> The volatile memory properties restrict them from low-power applications. While nonvolatile flash memories encounter charge storage problems originating from their fundamental scaling limits, which hinder their implementation on further size miniaturization.<sup>2</sup> To overcome the bottleneck, enormous emerging nonvolatile memories, such as phase change random access memory,<sup>3</sup> magnetoresistive RAM,<sup>4</sup> and resistive RAM (RRAM)<sup>5</sup> are viewed as the next promising candidates or alternatives by their excellent memory performance and requirements. Among them, RRAMs exhibit lots of benefits, including low fabrication cost, a simple metal–insulator–metal (MIM) structure, complementary metal–oxide–semiconductor compatibility, small effective cell size of  $4F^2$ , fast switching speed, high cycling endurance, and favorable retention time.<sup>6–8</sup> Transition metal oxide RRAMs such as HfO<sub>2</sub>,<sup>9,10</sup> TiO<sub>2</sub>,<sup>11,12</sup> NiO,<sup>13,14</sup> and ZnO<sup>15,16</sup> have been extensively studied and researched. In this study, a ternary compound (MgGa<sub>2</sub>O<sub>4</sub>)

serves as the resistive switching layer (SL). MgGa<sub>2</sub>O<sub>4</sub> is a partially inverse spinel with a lattice constant of 8.286 Å<sup>17</sup> and possesses good mechanical properties (no cleavage planes).<sup>18</sup> It is also a wide band gap ( $\sim 4.9$  eV at room temperature) metal oxide and a high melting point (1930 °C) material.<sup>19</sup> Galazka et al. demonstrate that the melt-grown MgGa<sub>2</sub>O<sub>4</sub> crystals could be either insulators or semiconductors, depending on the incorporation of oxygen during the growth atmosphere and the growth method.<sup>20</sup> The presence of oxygen results in an electrical insulator with relatively low electron mobility (a few cm<sup>2</sup> V<sup>-1</sup> s<sup>-1</sup>). Meanwhile, it can also be an excellent microwave material owing to its relative dielectric constant of 9.54, and materials based on MgGa<sub>2</sub>O<sub>4</sub> are used in microwave dielectrics, optoelectronics, and spintronics.<sup>21</sup> Many reported MgGa<sub>2</sub>O<sub>4</sub> works are related to phosphors (via doping) and investigate their illuminance characteristics.<sup>22,23</sup> Furthermore, MgGa<sub>2</sub>O<sub>4</sub> is used as a spinel barrier

Received: July 5, 2022

Accepted: January 5, 2023

Published: January 16, 2023



for magnetic tunnel junctions because of its low-resistance area product and favorable tunnel magnetoresistance ratio.<sup>24</sup> Meanwhile, MgO-based RRAM shows nonpolar switching characteristics,<sup>25</sup> and Ga<sub>2</sub>O<sub>3</sub>-based RRAM<sup>26</sup> also demonstrates feasibility for neuromorphic applications via quantum dots. For spinel MgGa<sub>2</sub>O<sub>4</sub>, the high bandgap could suppress current leakage during the off state. The good thermal stability (compared to  $\beta$ -MgGa<sub>2</sub>O<sub>4</sub>)<sup>20</sup> makes RRAM more stable during switching operations since the Joule heating effect occurs during the reset operation. The Joule heat might affect the resistive switching behaviors and stability of RRAMs in structures of 2D memory arrays and even in 3D architecture. The two aforementioned merits make it suitable for being fabricated as memory devices. To the best of our knowledge, memristors based on MgGa<sub>2</sub>O<sub>4</sub> have not been studied and reported. Our work aims to investigate whether this metal oxide possesses resistive switching characteristics and is a potential material for nonvolatile memory applications.

## EXPERIMENTS

The common bottom electrode (BE) RRAM is manufactured in the following steps. First, the glass substrate is cleaned by acetone, isopropyl alcohol, and deionized water in an ultrasonic cleaning machine in order to remove particles from the surface of the substrate. Second, the BE is deposited by the E-gun evaporation system. The 10 nm titanium (Ti) is deposited for the adhesion layer, and the 50 nm platinum is used as the BE. Third, the 40 nm SL is deposited by the RF magnetron sputtering system. The base pressure for fabrication is below 5  $\mu$ Torr, and the working pressure is fixed at 5 mTorr. The MgGa<sub>2</sub>O<sub>4</sub> target is prepared, and the three O<sub>2</sub>/(Ar + O<sub>2</sub>) ratio conditions are 0, 10, and 20%, respectively. Detailed fabrication conditions are listed in Table 1. Fourth, the top

**Table 1. MgGa<sub>2</sub>O<sub>4</sub>-Resistive Random-Access Memory Fabrication Parameters**

pressure	5 mTorr
oxygen partial pressure	0, 10, 20%
RF power	80 W
thickness	40 nm

electrode is deposited through a thermal evaporator, and the thickness is expected to be controlled at 60 nm. The shape and size of SLs and top electrodes are all defined by shadow masks.

Any lithography-related method is not used. To investigate how the different oxygen partial pressures influence the resistive switching behaviors, X-ray photoelectron spectroscopy (XPS: PHI 5000 VersaProbe) is carried out to identify the amount of oxygen vacancies under different O<sub>2</sub>/(Ar + O<sub>2</sub>) ratios. An ultrahigh resolution transmission electron microscope (TEM: JEOL JEM-2100F Cs STEM) is used to confirm the thickness of each layer and the cross-section structure of Al/MgGa<sub>2</sub>O<sub>4</sub>/Pt/Ti RRAM. Energy-dispersive X-ray spectroscopy (EDX) line scan analysis is used to identify the distribution of every element in the form of a MIM structure. The electrical characteristics of the RRAMs are evaluated using the B1500A semiconductor parameter analyzer, where the positive bias is applied on the top electrode while the BE is electrically grounded as reference. All the measurements are under a dark environment and at room temperature. Statistical analyses are also conducted to explore the distribution of resistance and programming voltage.

## RESULTS AND DISCUSSION

The schematic diagram of RRAM is shown in Figure 1, where the structure is a typical MIM structure. The cross-sectional TEM image in Figure 2 implies 62 nm Al (TE), 40 nm

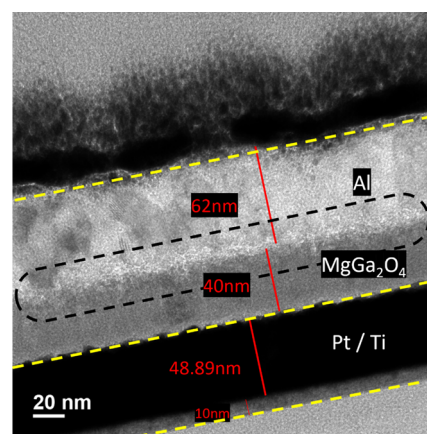


**Figure 2.** TEM cross-section of Al/MgGa<sub>2</sub>O<sub>4</sub>/Pt/Ti.

MgGa<sub>2</sub>O<sub>4</sub>, 48.89 nm Pt (BE), and the 10 nm Ti (adhesion layer), all of which are precisely controlled. Energy-dispersive spectroscopy line scan analysis shows the distribution of every

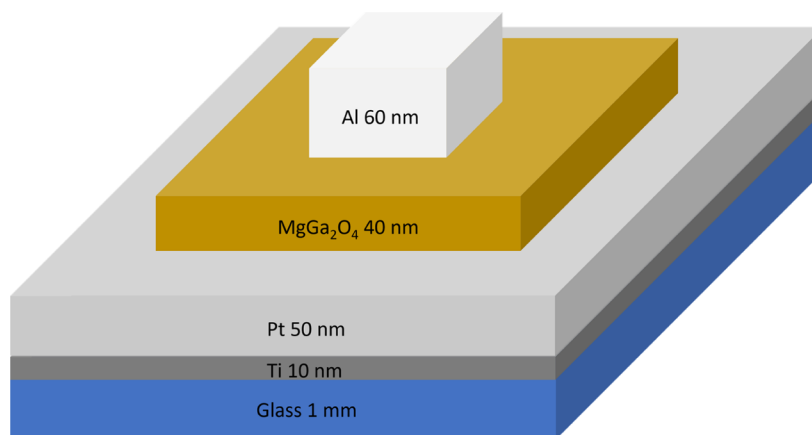


**Figure 1.** Schematic diagram of the MIM structure.

element within the Al/MgGa<sub>2</sub>O<sub>4</sub>/Pt/Ti/glass structure, as shown in Figure 3. For simplicity, we denote 0% O<sub>2</sub> as device

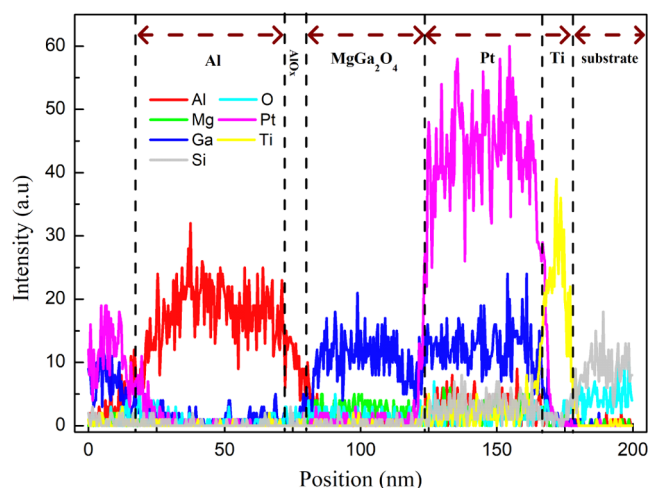


**Figure 3.** Line scan of EDX to demonstrate the distribution of each element.

A, 10% O<sub>2</sub> as device B, and 20% O<sub>2</sub> as device C. From voltage sweep results, device A does not demonstrate resistive

switching characteristics, while devices B and C show bipolar switching behavior. Their forming voltages are 21.9 and 15.0 V, as shown in Figure 4a, respectively. From Figure 4b,c, device B could repeatably change resistance states between high resistance states (HRS) and low-resistance states (LRS) for nearly 40 times. On the other side, device C could substantially improve endurance over 2000 switching cycles. The huge difference in reliability could be explained by the number of oxygen vacancies present in the SL. From the XPS data in Figure 5, O 1s peaks of 0, 10, and 20% MgGa<sub>2</sub>O<sub>4</sub> could be deconvoluted into three peaks around 531.0, 532.1, and 533.2 eV, which correspond to lattice oxygen (M–O), oxygen vacancy (V<sub>o</sub>), and the OH group (O<sub>H</sub>), respectively. The percentage of the lattice oxygen, oxygen vacancy, and OH group are the individual area divided by the total area of fitting data. The corresponding V<sub>o</sub> percentages are 12.32, 18.30, and 25.97% with the increasing oxygen partial pressure. Because of the shortage of high energy, little oxygen gas could effectively react with the metal atoms during the fabrication process since the deposition condition is nearly at room temperature. Thus, excess oxygen flux is viewed as the reason causing more oxygen-related defects. To further study the composition of elements, EDX in Table 2 is carried out to confirm the non-stoichiometric 20% O<sub>2</sub> thin film. The non-stoichiometric and oxygen-deficient MgGa<sub>2</sub>O<sub>4</sub> via the RF-sputtering method and

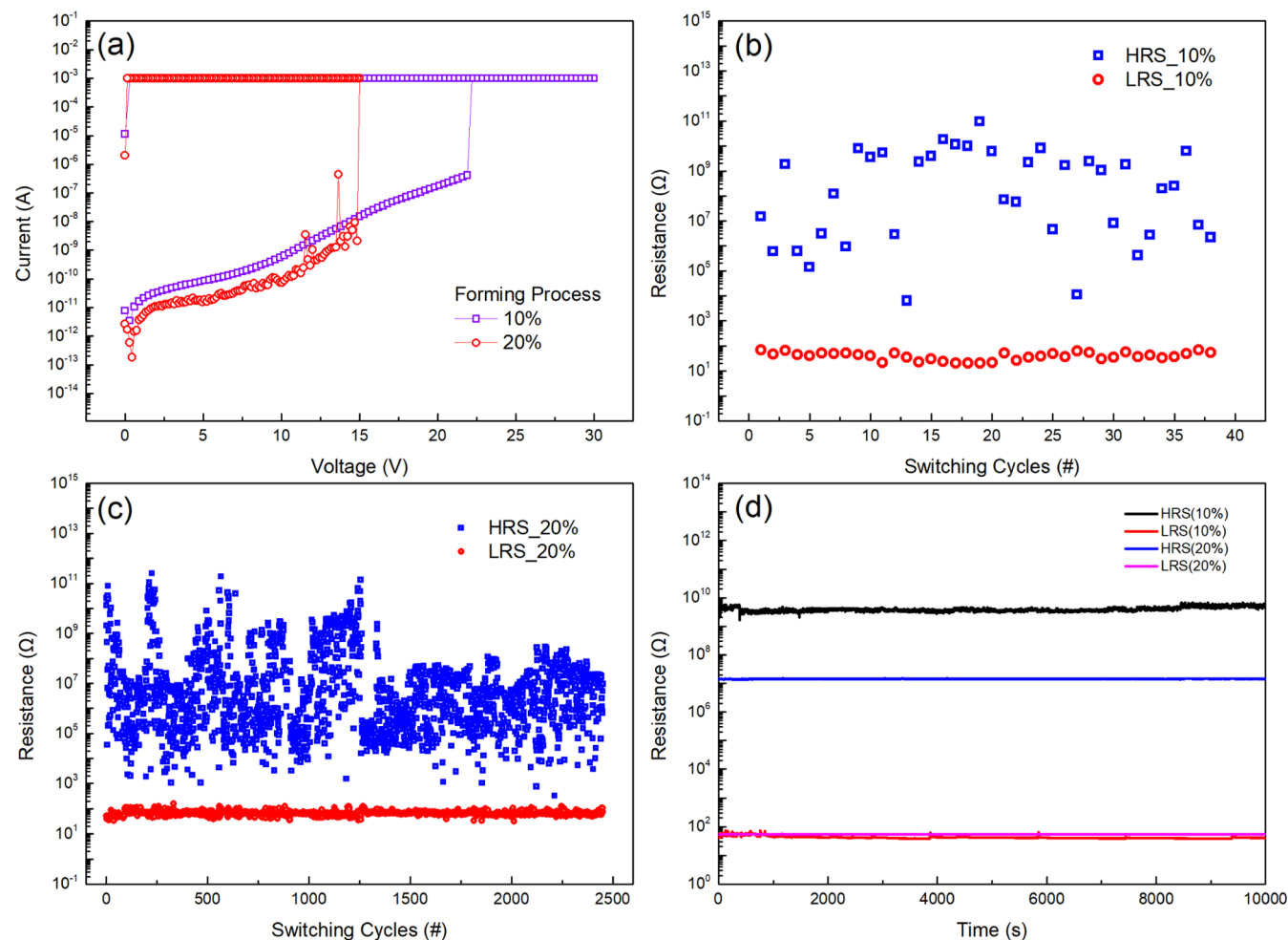


**Figure 4.** (a) Forming process of 10 and 20% RRAM. Current compliance is 1 mA to prevent hard breakdown. (b) Cycling endurance of 10% RRAM. (c) Cycling endurance of 20% RRAM. (d) Retention tests of 10 and 20% RRAMs for 10,000 s.

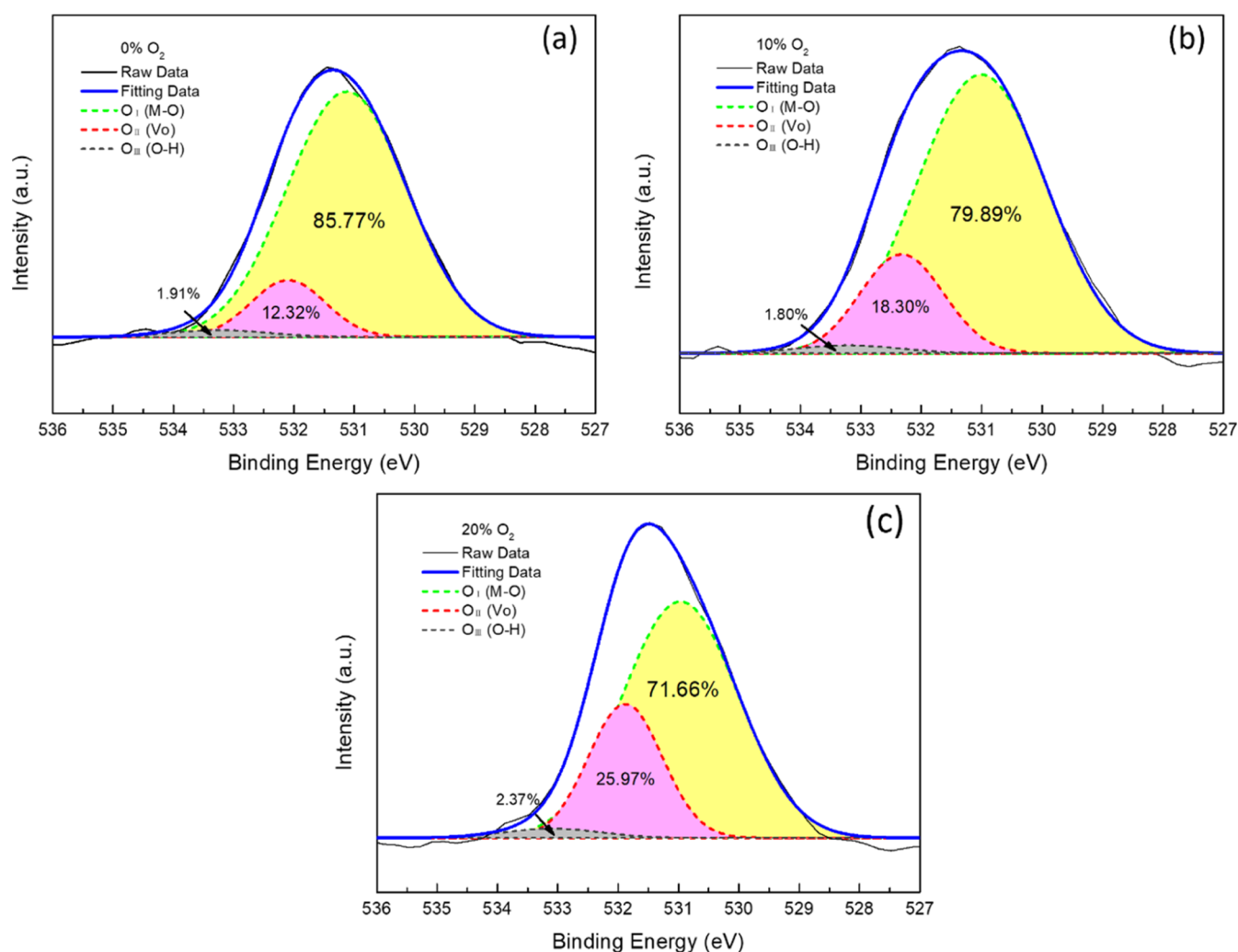


**Figure 5.** O 1s of MgGa<sub>2</sub>O<sub>4</sub> thin film, where the binding energies of the lattice oxygen, oxygen vacancy, and OH group are about 531.0, 532.1, and 533.2 eV, respectively. (a) 0% O<sub>2</sub>, (b) 10% O<sub>2</sub>, and (c) 20% O<sub>2</sub>.

**Table 2. Energy-Dispersive Spectroscopy Results**

element	EDX results		stoichiometry
	wt %	atom %	atom %
Mg	5.91	10.00	14.3
Ga	76.73	45.31	28.6
O	17.37	44.69	57.1
total	100	100	100

the fabrication condition cause a higher amount of V<sub>o</sub>, which is essential and beneficial for resistive switching.<sup>27,28</sup>

For the polarity of V<sub>Set</sub> and V<sub>Reset</sub>, RRAM can be classified as unipolar switching and bipolar switching.<sup>6</sup> The V<sub>Set</sub> and V<sub>Reset</sub> of a bipolar switching RRAM are on the opposite polarity of the applied voltage. While for unipolar switching RRAM, the polarity of V<sub>Set</sub> and V<sub>Reset</sub> is the same. From Figure 6, we could observe that the set transition occurs at the positive voltage, while the reset transition occurs at the negative polarity voltage. The bipolar switching-type RRAM with low-diffusivity metal electrodes typically uses oxygen vacancy filaments to account for the resistive switching phenomenon, where the oxygen vacancies play a crucial role of RS. The fabrication conditions of the SL and the number of oxygen vacancies will intensively influence the RS characteristics. Besides, the EDX

line scan analysis reveals that there are no apparent Al atoms detected in our SL. Therefore, it is reasonable to utilize the valence change memory (VCM) model to explain the switching mechanism of our RRAMs with the Al top electrode.

The process by which VCMs alter resistance between two states is shown in Figure 7. The red arrow points in the direction of the electric field during the set and reset operation. Al with relatively low-standard Gibbs free energy (−1582.9 kJ/mol) intends to induce the formation of an interfacial layer (AlO<sub>x</sub>).<sup>29</sup> Meanwhile, the EDX line scan results indicate the existence of a transition region (AlO<sub>x</sub>) between Al and MgGa<sub>2</sub>O<sub>4</sub>. In contrast, the interface of Pt (BE) demonstrates a steep curve, indicating that MgGa<sub>2</sub>O<sub>4</sub> hardly reacts with Pt. Thus, the IL (AlO<sub>x</sub>) should be taken into account for the involvement of resistive switching as well. Initially, the MgGa<sub>2</sub>O<sub>4</sub> RRAM is in its pristine state; after a forming process (soft dielectric breakdown), the oxygen ions (O<sup>2−</sup>) progressively accumulate at the top electrode due to the electric field from the TE to the BE and leave the oxygen vacancies in the SL. Filaments composed of oxygen vacancies gradually take shape under the high electric field. Eventually, oxygen vacancies are connected between BE and TE, which makes the resistance of MgGa<sub>2</sub>O<sub>4</sub> RRAM become a LRS. The alignment of oxygen vacancies forms a conductive channel and

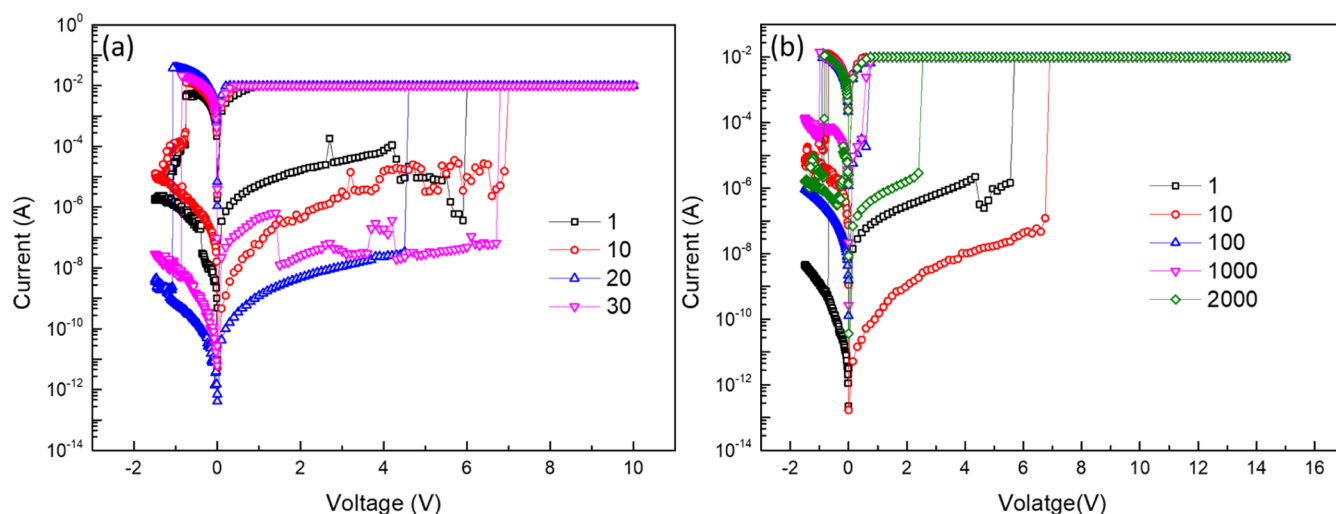


**Figure 6.** Current to voltage characteristic curve of (a) 10%  $\text{MgGa}_2\text{O}_4$  RRAM and (b) 20%  $\text{MgGa}_2\text{O}_4$  RRAM.

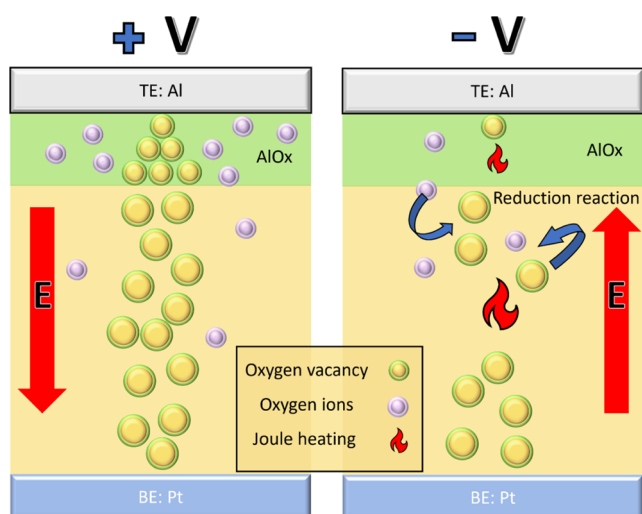


**Figure 7.** Schematic diagram for the set and reset mechanisms during set and reset operations.

allows a great deal of current to flow through. After a reset operation enforcing the rupture of the filament, the resistance is back to HRS. The occurrence of this phenomenon is mainly due to the applied negative voltage repelling the oxygen ions from the TE and the oxygen reservoir layer ( $\text{AlO}_x$ ), which then recombine with the oxygen vacancies and promote the breakage of conductive filaments in the SL. Besides, the Joule heating effect could also be discovered from the abrupt current reduction at the reset voltage, which helps to partially rupture the conductive filaments.<sup>30</sup> The generation of oxygen vacancies ( $V_o$ ) and disintegration of conductive filaments cause RRAM to switch between two states consecutively.

From Figure 4b,c, a widely high-resistance state distribution is observed in both device B and device C. The relatively higher distributed HRS ranging approximately from  $10^3$  to  $10^{11} \Omega$  is probably attributed to the gap length<sup>31</sup> variation and the partial fracture of conductive filaments during each reset operation. Filaments being ruptured with a longer gap length give rise to a longer  $V_o$ -scarce region and cause a relatively higher HRS, while the relatively lower HRS is due to the shorter gap region resulting in a smaller resistance. We believe that the highly distributed HRS is owing to the formation of

the interfacial layer ( $\text{AlO}_x$ ) and the random growth and rupture of conductive filaments composed of oxygen vacancies in our SLs.

The endurance tests for both device B and device C are shown in Figure 4b,c; large resistance ratios are obtained for both devices. However, there still exist some low HRS points owing to incomplete fracture of filaments. Statistical plots regarding the resistance distribution and programming voltages are shown in Figure 8, and the average values of the set voltage are 5.27 and 3.23 V with a standard deviation of 2.01 and 1.85 V, respectively. On the other hand, the amplitude of the reset voltages and the standard deviation for both devices are very close. Comparing the two devices, 20%  $\text{O}_2$  RRAM exhibits a lower and more concentrated  $V_{\text{Set}}$  and substantially improved reliability, which is better than 10% of the  $\text{O}_2$  device. Wide and highly random distribution of HRS and  $V_{\text{Set}}$  should be avoided regarding memory application. However, it is suitable for physical unclonable function applications owing to the high randomness between each switching cycle.<sup>32</sup>

The retention tests for device B and device C are also conducted to confirm the data retention capacity. Figure 4d shows the  $\text{MgGa}_2\text{O}_4$  RRAM could sustain its current state for 10,000 s without apparent degradation. The reading voltage is set up as 20 mV to prevent altering the present resistance state. It is worth noting that a higher HRS usually produces a larger set voltage, as shown in Figure 9. The Pearson product-moment correlation coefficient between the set voltage and HRS is approximately 0.66, indicating a strong correlation between them. Since for a higher HRS represents a more isolated distribution of oxygen vacancies in SL. Scarce oxygen vacancies demand a higher electric field to rearrange the growth of conductive filaments. The detailed extracted performance parameters of three oxygen partial pressure RRAMs are listed in Table 3 for comparison.

To clarify the conduction mechanism behind the  $\text{MgGa}_2\text{O}_4$  RRAM, double logarithmic  $I$ - $V$  curves are used to fit the experimental data, as shown in Figure 10. The LRS of both set and reset operations all follows ohmic conduction with a slope of approximately 1. The conduction mechanism of HRS is divided into three regions: at the low voltage region, thermally generated carriers dominate the conduction mechanism. Therefore, the current is approaching linearly proportional to the applied voltage, which follows ohmic conduction. For the

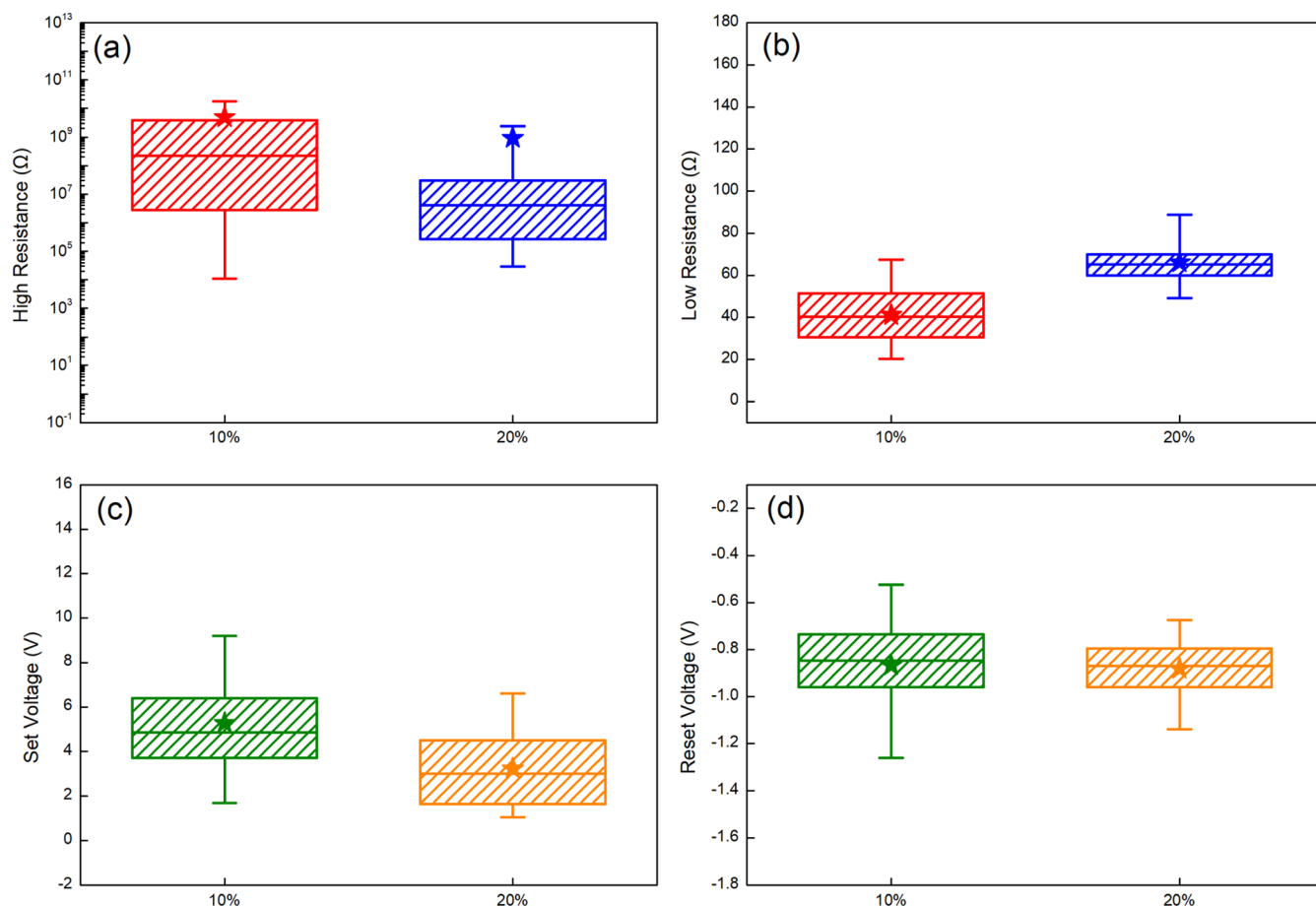


**Figure 8.** Box chart for the resistance state and programming voltage distributions of  $\text{MgGa}_2\text{O}_4$  RRAM. (Where the top line, star, box, and bottom line represent 95%, mean, 75, 50, 25, and 5% of the entire distribution). (a) High-resistance distribution. (b) Low-resistance distribution. (c) Set voltage distribution. (d) Reset voltage distribution.

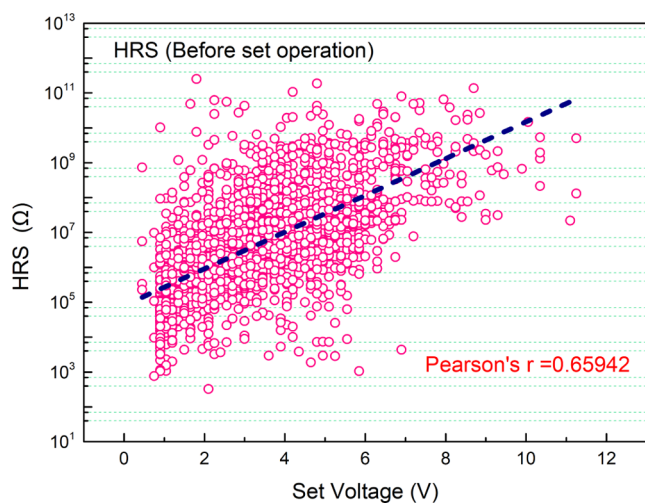


**Figure 9.** Correlation between HRS and the next time set voltage.

intermediate voltage region, the injected electrons from the electrode exceed thermally generated electrons. The slope turns to 1.934 and 2, corresponding to the trap-limited space charge limited conduction (SCLC).<sup>33</sup> Finally, at a high electric field region, the slope is about 3.888, corresponding to the trap-filled SCLC region.<sup>34</sup> For negative voltage sweep, the applied voltage is not as high as for set operation; hence, the trap-filled SCLC does not appear in Figure 10b.

## CONCLUSIONS

In this experiment, we fabricate RRAMs with three kinds of oxygen partial pressure conditions, where the top electrodes are made of Al. The 20%  $\text{O}_2$  RRAM could sustain over 2000 switching cycles due to its proper number of oxygen vacancies and the easier growth of the conductive filament. Therefore, the control of the defect concentration in the SL and interface is very crucial for reliability. Statistical analysis reveals that the  $\text{MgGa}_2\text{O}_4$  RRAM with the Al top electrode exhibits highly distributed HRS, which is attributed to the formation of the  $\text{AlO}_x$  layer and the participation of the Joule heating effect. The

**Table 3.** Comparison of Performance Parameters of RRAMs under Different Oxygen Partial Pressure Conditions

oxygen partial pressure (%)	no. of cycles	$V_{\text{forming}}$ (V)	$V_{\text{Set (avg.)}}$ (V)	SD of $V_{\text{Set}}$ (V)	$V_{\text{Reset (avg.)}}$ (V)	SD of $V_{\text{Reset}}$ (V)	retention (s)
0							
10	38	21.9	5.27	2.01	−0.87	0.19	10,000
20	2451	15.0	3.23	1.85	−0.88	0.14	10,000

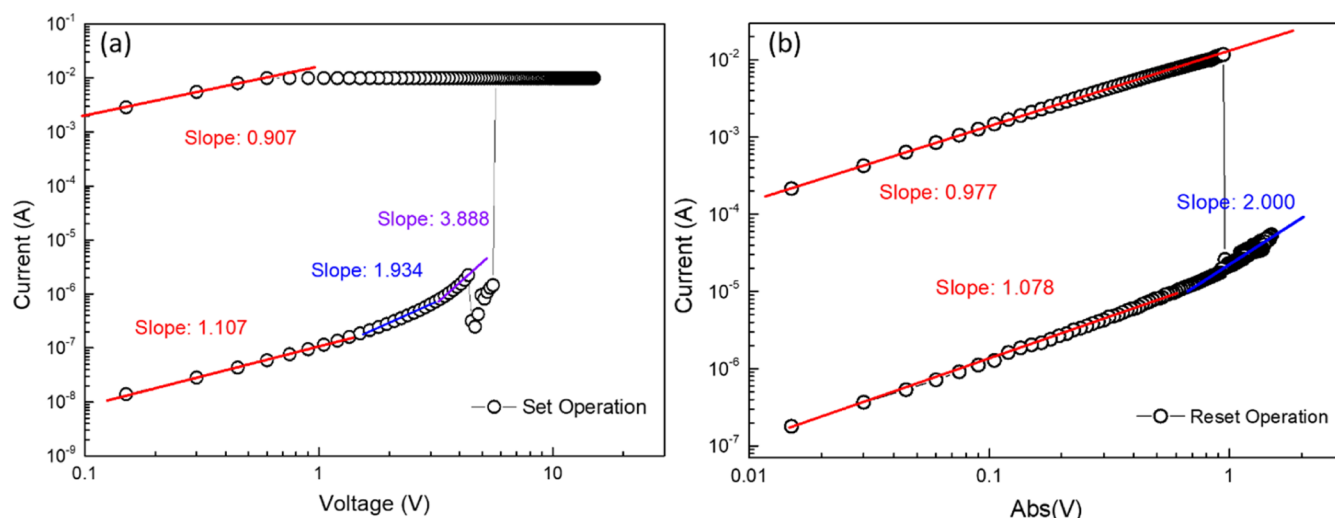


**Figure 10.** Current–voltage fitting curve of 20% MgGa<sub>2</sub>O<sub>4</sub> RRAM. (a) Positive bidirectional voltage sweeps for set operation in the range of 0–15 V. (b) Negative bidirectional voltage sweeps for reset operation in the range of 0 to –1.5 V.

investigation of the current conduction mechanism is also carried out by means of a double logarithmic  $I$ – $V$  plot, where LRS and HRS correspond to ohmic conduction and SCLC separately. In general, the MgGa<sub>2</sub>O<sub>4</sub> with the Al electrode demonstrates high endurance reliability and data retention capacity. However, it still suffers from huge fluctuations during every switching cycle, which leaves room for further improvements when utilized as memory storage devices.

## AUTHOR INFORMATION

### Corresponding Author

Sheng-Po Chang – Department of Photonics, National Cheng Kung University, Tainan City 70101, Taiwan; [orcid.org/0000-0002-4126-0576](https://orcid.org/0000-0002-4126-0576); Phone: +886-6-275-7575 extn 62400-1208; Email: [changsp@mail.ncku.edu.tw](mailto:changsp@mail.ncku.edu.tw)

### Authors

Yu-Neng Kao – Institute of Microelectronics & Department of Electrical Engineering, National Cheng Kung University, Tainan City 70101, Taiwan

Wei-Lun Huang – Institute of Microelectronics & Department of Electrical Engineering, National Cheng Kung University, Tainan City 70101, Taiwan

Wei-Chih Lai – Department of Photonics, National Cheng Kung University, Tainan City 70101, Taiwan; [orcid.org/0000-0003-2703-8845](https://orcid.org/0000-0003-2703-8845)

Shouu-Jinn Chang – Institute of Microelectronics & Department of Electrical Engineering, National Cheng Kung University, Tainan City 70101, Taiwan

Complete contact information is available at:

<https://pubs.acs.org/10.1021/acsomega.2c04222>

### Author Contributions

Y.N.K., W.L.H., S.P.C., W.C.L., and S.J.C. contributed equally to this work; Y.N.K. and S.P.C. wrote the paper.

### Notes

The authors declare no competing financial interest.

## ACKNOWLEDGMENTS

The authors would like to thank the Ministry of Science and Technology, Taiwan, for financially supporting this research

under contract no. MOST 109-2221-E-006-203-MY3 and 110-2218-E-006-025-MBK. The authors gratefully acknowledge the use of JEOL JEM-2100F CS STEM equipment belonging to the Instrument Center of National Cheng Kung University.

## REFERENCES

- Bez, R.; Camerlenghi, E.; Modelli, A.; Visconti, A. Introduction to Flash memory. *Proc. IEEE* **2003**, *91*, 489–502.
- Strukov, D. B.; Snider, G. S.; Stewart, D. R.; Williams, R. S. The missing memristor found. *Nature* **2008**, *453*, 80–83.
- Liu, B.; Wei, T.; Hu, J.; Li, W.; Ling, Y.; Liu, Q.; Cheng, M.; Song, Z. Universal memory based on phase-change materials: From phase-change random access memory to optoelectronic hybrid storage. *Chin. Phys. B* **2021**, *30*, 058504.
- Nisar, A.; Dhull, S.; Kaushik, B. K.; Mittal, S. High-performance voltage controlled multilevel MRAM cell. *Semicond. Sci. Technol.* **2021**, *36*, 125013.
- Fang, Y.; Zhai, S.; Chu, L.; Zhong, J. Advances in halide perovskite memristor from lead-based to lead-free materials. *ACS Appl. Mater. Interfaces* **2021**, *13*, 17141–17157.
- Zahoor, F.; Zulkifli, T. Z. A.; Khanday, F. A. Resistive Random Access Memory (RRAM): an Overview of Materials, Switching Mechanism, Performance, Multilevel Cell (mlc) Storage, Modeling, and Applications. *Nanoscale Res. Lett.* **2020**, *15*, 26.
- Bricalli, A.; Ambrosi, E.; Laudato, M.; Maestro, M.; Rodriguez, R.; Ielmini, D. SiO<sub>x</sub>-based resistive switching memory (RRAM) for crossbar storage/select elements with high on/off ratio. *2016 IEEE International Electron Devices Meeting (IEDM)*; IEEE, 2016; pp 4.3.1–4.3.4.
- Ielmini, D. Resistive switching memories based on metal oxides: mechanisms, reliability and scaling. *Semicond. Sci. Technol.* **2016**, *31*, 063002.
- Roy, S.; Niu, G.; Wang, Q.; Wang, Y.; Zhang, Y.; Wu, H.; Zhai, S.; Shi, P.; Song, S.; Song, Z.; Ye, Z.-G.; Wenger, C.; Schroeder, T.; Xie, Y.-H.; Meng, X.; Luo, W.; Ren, W. Toward a reliable synaptic simulation using Al-doped HfO<sub>2</sub> RRAM. *ACS Appl. Mater. Interfaces* **2020**, *12*, 10648–10656.
- Chen, Y. Y.; Goux, L.; Clima, S.; Govoreanu, B.; Degraeve, R.; Kar, G. S.; Fantini, A.; Groeseneken, G.; Wouters, D. J.; Jurczak, M. Endurance/Retention Trade-off on HfO<sub>2</sub>/Metal Cap 1T1R Bipolar RRAM. *IEEE Trans. Electron Devices* **2013**, *60*, 1114–1121.
- Hsu, C. W.; Hou, T. H.; Chen, M. C.; Wang, I. T.; Lo, C. L. Bipolar NTiO<sub>2</sub>HfO<sub>2</sub>/Ni RRAM with multilevel states and self-rectifying characteristics. *IEEE Electron Device Lett.* **2013**, *34*, 885–887.

- (12) Jeong, H. Y.; Kim, Y. I.; Lee, J. Y.; Choi, S.-Y. A low-temperature-grown TiO<sub>2</sub>-based device for the flexible stacked RRAM application. *Nanotechnology* **2010**, *21*, 115203.
- (13) Wang, H.; Zou, C.; Zhou, L.; Tian, C.; Fu, D. Resistive switching characteristics of thin NiO film based flexible nonvolatile memory devices. *Microelectron. Eng.* **2012**, *91*, 144–146.
- (14) Chu, J.; Li, Y.; Fan, X.; Shao, H.; Duan, W.; Pei, Y. Multistate data storage in solution-processed NiO-based resistive switching memory. *Semicond. Sci. Technol.* **2018**, *33*, 115007.
- (15) Won Seo, J.; Baik, S. J.; Kang, S. J.; Hong, Y. H.; Yang, J. H.; Lim, K. S. A ZnO cross-bar array resistive random access memory stacked with heterostructure diodes for eliminating the sneak current effect. *Appl. Phys. Lett.* **2011**, *98*, 233505.
- (16) Wu, J.-L.; Chen, Y.-C.; Lin, H.-Y.; Chu, S.-Y.; Chang, C.-C.; Wu, C.-J.; Juang, Y.-D. Effect of ZnO Buffer Layer on the Bending Durability of ZnO:Ga Films Grown on Flexible Substrates: Investigation of Surface Energy, Electrical, Optical, and Structural Properties. *IEEE Trans. Electron Devices* **2013**, *60*, 2324–2330.
- (17) Sharma, G.; Castro, R. H. Synthesis and surface enthalpy of MgGa<sub>2</sub>O<sub>4</sub> spinel. *Thermochim. Acta* **2017**, *655*, 326–330.
- (18) Hirschle, C.; Schreuer, J.; Galazka, Z. Interplay of cation ordering and thermoelastic properties of spinel structure MgGa<sub>2</sub>O<sub>4</sub>. *J. Appl. Phys.* **2018**, *124*, 065111.
- (19) Galazka, Z.; Ganschow, S.; Irmscher, K.; Klimm, D.; Albrecht, M.; Schewski, R.; Pietsch, M.; Schulz, T.; Dittmar, A.; Kwasniewski, A.; et al. Bulk single crystals of  $\beta$ -Ga<sub>2</sub>O<sub>3</sub> and Ga-based spinels as ultra-wide bandgap transparent semiconducting oxides. *Prog. Cryst. Growth Charact. Mater.* **2021**, *67*, 100511.
- (20) Galazka, Z.; Klimm, D.; Irmscher, K.; Uecker, R.; Pietsch, M.; Bertram, R.; Naumann, M.; Albrecht, M.; Kwasniewski, A.; Schewski, R.; Bickermann, M. MgGa<sub>2</sub>O<sub>4</sub> as a new wide bandgap transparent semiconducting oxide: growth and properties of bulk single crystals. *Phys. Status Solidi A* **2015**, *212*, 1455–1460.
- (21) Jacob, K.; Sivakumar, S. Thermodynamic properties of MgGa<sub>2</sub>O<sub>4</sub> and phase relations in the system Mg-Ga-O. *J. Alloys Compd.* **2019**, *775*, 1357–1364.
- (22) Kudo, H.; Kitaya, M.; Kobayashi, H.; Shirai, M.; Tanaka, K.; Kawabe, Y.; Hanamura, E. Luminescence channels of manganese-doped MgGa<sub>2</sub>O<sub>4</sub>. *J. Phys. Soc. Jpn.* **2006**, *75*, 014708.
- (23) Zhao, Y.; Du, J.; Wu, X.; Wang, Y.; Poelman, D. Enhanced near-infrared persistent luminescence in MgGa<sub>2</sub>O<sub>4</sub>:Cr<sup>3+</sup> through codoping. *J. Lumin.* **2020**, *220*, 117035.
- (24) Sukegawa, H.; Kato, Y.; Belmoubarik, M.; Cheng, P.-H.; Daibou, T.; Shimomura, N.; Kamiguchi, Y.; Ito, J.; Yoda, H.; Ohkubo, T.; Mitani, S.; Hono, K. MgGa<sub>2</sub>O<sub>4</sub> spinel barrier for magnetic tunnel junctions: Coherent tunneling and low barrier height. *Appl. Phys. Lett.* **2017**, *110*, 122404.
- (25) Huang, H.-H.; Shih, W.-C.; Lai, C.-H. Nonpolar resistive switching in the Pt/MgO/Pt nonvolatile memory device. *Appl. Phys. Lett.* **2010**, *96*, 193505.
- (26) Yan, X.; Pei, Y.; Chen, H.; Zhao, J.; Zhou, Z.; Wang, H.; Zhang, L.; Wang, J.; Li, X.; Qin, C.; et al. Self-Assembled Networked PbS Distribution Quantum Dots for Resistive Switching and Artificial Synapse Performance Boost of Memristors. *Adv. Mater.* **2019**, *31*, 1805284.
- (27) Stevens, J. E.; Lohn, A. J.; Decker, S. A.; Doyle, B. L.; Mickel, P. R.; Marinella, M. J. Reactive sputtering of substoichiometric Ta<sub>2</sub>O<sub>x</sub> for resistive memory applications. *J. Vac. Sci. Technol., A* **2014**, *32*, 021501.
- (28) Lanza, M.; Wong, H. S. P.; Pop, E.; Ielmini, D.; Strukov, D.; Regan, B. C.; Larcher, L.; Villena, M. A.; Yang, J. J.; Goux, L.; et al. Recommended Methods to Study Resistive Switching Devices. *Adv. Electron. Mater.* **2019**, *5*, 1800143.
- (29) Li, Q.; Qiu, L.; Wei, X.; Dai, B.; Zeng, H. Point contact resistive switching memory based on self-formed interface of Al/ITO. *Sci. Rep.* **2016**, *6*, 29347.
- (30) Zhou, P.; Ye, L.; Sun, Q. Q.; Wang, P. F.; Jiang, A. Q.; Ding, S. J.; Zhang, D. W. Effect of concurrent joule heat and charge trapping on RESET for NbAlO fabricated by atomic layer deposition. *Nanoscale Res. Lett.* **2013**, *8*, 91.
- (31) Kumar, D.; Aluguri, R.; Chand, U.; Tseng, T.-Y. Metal oxide resistive switching memory: materials, properties and switching mechanisms. *Ceram. Int.* **2017**, *43*, S547–S556.
- (32) Chen, A. Utilizing the variability of resistive random access memory to implement reconfigurable physical unclonable functions. *IEEE Electron Device Lett.* **2015**, *36*, 138–140.
- (33) Kwan, C.-P.; Street, M.; Mahmood, A.; Echtenkamp, W.; Randle, M.; He, K.; Nathawat, J.; Arabchigavkani, N.; Barut, B.; Yin, S.; et al. Space-charge limited conduction in epitaxial chromia films grown on elemental and oxide-based metallic substrates. *AIP Adv.* **2019**, *9*, 055018.
- (34) Lim, E. W.; Ismail, R. Conduction Mechanism of Valence Change Resistive Switching Memory: A Survey. *Electronics* **2015**, *4*, 586–613.